Incorporation of tetrahedral ferric iron in hydrous ringwoodite

Word Count (excluding abstract, figure captions and references): 5938

Andrew R. Thomson[1,2*], Ross O. Piltz[3], Wilson A. Crichton[2], Valerio Cerantola[3,4], Isra S. Ezad[1,5], David P. Dobson[1,6], Ian G. Wood[1] and John P. Brodholt[1,7]

[1]*Department of Earth Sciences, University College London, London, WC1E 6BT.*

[2]*ESRF- The European Synchrotron, 38043 Grenoble, France*

[3]*Bragg Institute, Australian Nuclear Science and Technology Organisation, Australia.*

[4]*European X-ray free-electron laser, Hamburg, Germany*

[5]*Department of Earth and Environmental Sciences, Macquarie University. Australia*

[6]*Bayeriches Geoinstitut, University of Bayreuth, 95440 Bayreuth, Germany.*

[7]*Centre for Earth Evolution and Dynamics, University of Oslo, N-0316 Oslo, Norway*

*Corresponding Author (a.r.thomson@ucl.ac.uk)

ABSTRACT

Hydrous Fo_{91} ringwoodite crystals were synthesised at 20 GPa and high-temperature conditions using a multi-anvil press. Recovered crystals were analysed using electron microprobe analysis, Raman spectroscopy, infrared spectroscopy, synchrotron Mössbauer spectroscopy, single-crystal X-ray diffraction and single-crystal Laue neutron diffraction, to carefully characterise the chemistry and crystallography of the samples. Analysis of the combined datasets provides evidence for the presence of tetrahedrally coordinated ferric iron and multiple hydrogen incorporation mechanisms within these blue-coloured iron-bearing ringwoodite crystals. Tetrahedral ferric iron is coupled with cation disorder of silicon onto the octahedrally coordinated site. Cation disorder in mantle ringwoodite minerals may be promoted in the presence of water, which could have implications for current models of seismic velocities within the transition zone. Additionally, the presence of tetrahedrally coordinated ferric iron may cause the blue colour of many ringwoodite, and other high-pressure, crystals.

Keywords:

- Ringwoodite
- Single-crystal diffraction
- Mössbauer spectroscopy

INTRODUCTION

The Earth's transition zone (TZ), delineated by global seismic velocity discontinuities at ~ 410 and 660 km depth (Dziewonski and Anderson 1981), has the potential to be Earth's largest volatile reservoir with a maximum water storage capacity greater than the entirety of surface reservoirs (Jacobsen 2005). This is possible because wadsleyite and ringwoodite, high-pressure polymorphs forming after olivine, constitute over 60 wt.% of TZ phase assemblages, and are capable of incorporating up to 3.3 wt.% and ~ 2 wt.% H_2O respectively (33,000 and 20,000 wt. ppm)[i] associated with point defects (e.g. Smyth 1987; Inoue et al. 1995; Ye et al. 2012; Fei and Katsura 2020). Whilst experiments clearly demonstrate the potential for TZ water storage, whether or not Earth's mantle is actually hydrated, and exactly how this water is incorporated in TZ minerals, continue to be the subjects of ongoing research.

There is significant variation between the range of estimates for the TZ's water content. A natural single crystal of ringwoodite, trapped as a mineral inclusion in a Brazilian diamond, was estimated, via FTIR, to contain ~ 1.4 wt.% H_2O (Pearson et al. 2014; Thomas et al. 2015). This observation suggests that the TZ is at least locally hydrated. However, it is unclear how this isolated observation from a microscopic diamond-hosted inclusion might relate to the bulk water content of the TZ more globally. Seismological studies aiming to constrain the water content of the TZ to-date have remained inconclusive, variously suggesting that both a dry (< 0.1 wt. % H_2O) or wet (~ 1 wt.% H_2O) TZ might be consistent with observations based on seismic velocities as well as the depths and magnitudes of discontinuities (van der Meijde 2003; Meier et al. 2009; Suetsugu et al. 2010; Houser 2016). Interpretations of water contents using magnetotelluric (MT) observations are inconsistent, and suggest the TZ contains between 0.001 and 1 wt.% H_2O (Karato and Wu 1993; Huang et al. 2005;

[i] Whilst it is convention to discuss the "water content" of hydrous and nominally anhydrous Earth-forming minerals, there is not actually additional water molecules (H_2O) stored in these phases. Instead hydrogen is incorporated in association with various cation defects in the "anhydrous" crystal structure, thus it would be more technically accurate to discuss the "proton" or "hydrogen" content of these samples.

Yoshino et al. 2008; Munch et al. 2020). Alternatively, explanation of mantle viscosity profiles seem to require the TZ to be close to water saturation, based on constraints from rheological experiments (Fei et al. 2017). Irrespective of the true TZ water content, understanding the incorporation mechanisms of hydrogen in crystals of wadsleyite and/or ringwoodite is important since, even at low concentrations, defects are known to affect fundamental physical properties vital for understanding the mechanics of mantle convection, e.g. viscosity, conductivity and elasticity (Thomas et al. 2012; Hustoft et al. 2013; Schulze et al. 2018).

Compared to the defect chemistry of wadsleyite, which is relatively well understood and in which protons almost exclusively substitute for Mg^{2+} vacancies (Smyth 1994), the behaviour of ringwoodite is less well constrained (Kudoh et al. 2000; Smyth et al. 2003). Previous studies variously using ab initio calculations, X-ray diffraction, spectroscopy (including at low temperatures) and ^{1}H NMR have concluded that a combination of multiple hydrogen incorporation mechanisms occur in ringwoodite (Smyth et al. 2003; Blanchard et al. 2009; Panero et al. 2013; Grüninger et al. 2017). Suggested substitutions include those where hydrogen is charge balanced by Mg^{2+} or Si^{4+} vacancies alone, but also have included more complex mechanisms involving Si-Mg cation disorder. The extremely disordered O-H stretching region observed in FTIR spectra of ringwoodite attests to the complexity of water incorporation mechanisms in ringwoodite (Kudoh 2001; Smyth et al. 2003; Blanchard et al. 2009; Panero 2010), which is discussed far more extensively later in this paper. To date only two experimental studies have attempted to directly investigate the hydrogen incorporation mechanisms in iron-free ringwoodite, one using ^{1}H solid state NMR (Grüninger et al. 2017) and the other time-of-flight single-crystal neutron diffraction (Purevjav et al. 2018). No published studies have directly investigated the incorporation mechanism of water in iron-bearing ringwoodite samples; this study was an attempt to do this.

We present analyses of Fo_{91} ringwoodite crystals using a variety of techniques, which were all performed on crystals synthesised in a single high-pressure experiment. Employing Electron Probe

Micro Analysis (EPMA), Raman, Infrared and Synchrotron Mössbauer Spectroscopy (SMS), the chemistry, water content and ferric/ferrous iron ratio of the samples were determined prior to diffraction data. Subsequently single-crystal X-ray diffraction and Neutron Laue diffraction data were collected from the synthetic samples. This combination of analytical techniques provides new insights into the crystallography of hydrous iron-bearing ringwoodite, which may be a major component of mantle assemblages throughout the transition zone.

METHODS

Sample synthesis

The ringwoodite crystals investigated in the present study were synthesised in a single multi-anvil experiment using a 5000 tonne multi-anvil press at the Bayerisches Geoinstitut. The starting material consisted of synthetic brucite ($Mg(OH)_2$), FeO and SiO_2, to form a Fo_{90} olivine composition, and contained 5 wt.% H_2O. This material was packed in a 2.0 mm diameter Pt capsule, welded shut, and loaded into an 18 mm Cr-doped MgO octahedron with a $LaCrO_3$ heater. 54 mm WC carbide cubes with 8 mm truncations were used to generate the sample pressure. Conditions of approximately 20 GPa and 1470 °C were maintained for 30 minutes before slowly cooling to 1150 °C over 6.5 hours at which point the temperature was rapidly quenched and pressure slowly released. The recovered capsule was opened and blue crystals (figure 1), ranging in size up to ~ 0.5 x 0.5 x 0.5 mm, were recovered. It is noted that different individual crystals, but all from this single high-pressure experiment, were analysed throughout this study. Small fractions of what was, presumably, quenched melt were observed on the capsule walls.

Infrared, Raman and Mössbauer spectroscopy

Fourier transform infrared (FTIR) spectra were collected from doubly-polished single-crystal wafers of 40-60 μm thickness using a Thermo Scientific iN10 MX instrument operated in transmission mode at

University College London. Incident beam size was controlled using motorised apertures, and varied from 30 x 30 μm to 100 x 100 μm. Unpolarised spectra were collected between 675 and 7000 cm^{-1} from three randomly oriented crystals through a CaF_2 substrate (figure 2b). Sample thicknesses were measured using a reflected light microscope with calibrated z-motion, and are estimated to be accurate to within ± 2 μm (uncertainty of ~ ± 3.5 – 4.8 %). Raman spectra, with 4 cm^{-1} resolution using a 532 nm excitation laser (figure 2a), were collected using a WiTek Raman system in the Department of Earth Sciences, University College London, UK.

Energy-domain Mössbauer transmission spectroscopy was performed on a single ringwoodite crystal (~ 100 x 100 x 100 μm in size) at the nuclear resonance beamline ID18 at European Synchrotron Radiation Facility (ESRF) using the synchrotron Mössbauer source (SMS) (Potapkin et al. 2012). The velocity scales of all Mössbauer spectra were calibrated relative to 25 μm-thick α-Fe foil, and all spectra were fitted using the software package MossA (Prescher et al. 2012).

Electron probe micro analysis

The major element chemistry of several crystals from within the recovered products was determined with wavelength-dispersive spectroscopy using the Field Emission Gun Jeol JXA8530F Hyperprobe situated in the School of Earth Sciences at the University of Bristol. In preparation for these analyses, approximately ten ringwoodite crystals from the synthesis products were randomly picked, mounted in epoxy, and polished using a range of grits down to 0.25 μm diamond paste. Samples were carbon coated alongside a range of natural silicate and metal standards, beam conditions used were 15 keV and 10 nA, and the calibrations were verified by analysing a range of in-house secondary standards prior to analysing samples. Suitable crystals (a total of eight) were analysed in multiple locations using a 30 nm incident electron beam, resulting in a spatial resolution of ~ 2 microns at the sample surface. Data were reduced using a Phi-Rho-Z scheme accounting for the ferric iron (rounded to the nearest absolute 10 %) and water contents measured by SMS and difference from 100 % total respectively.

Analyses with totals outside 98-100 wt.% (~ 99 – 101 wt.% after accounting for water incorporation as quantified by FTIR) were rejected.

X-ray and Neutron diffraction

Single-crystal X-ray diffraction data were collected from a randomly selected crystal (~ 100 x 100 x 100 μm in size) using the standard setup on beamline ID15B of the ESRF. A monochromatic x-ray beam (λ=0.410884 Å) of 10 x 10 μm size was used in conjunction with a MAR555 detector to collect diffraction data in a ± 40° ϕ scan, integrating over 0.5° increments, Merlini & Hanfland (2013). Integration of the reflection intensities and absorption corrections were performed using CrysAlisPro (RED 171.32.29) software, prior to averaging and structure refinement using Jana2006, Petříček et al. (2014).

Single-crystal Laue neutron diffraction of a large (~ 500 x 500 x 500 μm) crystal was performed on the KOALA instrument on the reactor neutron source at the Australian Nuclear Science and Technology Organisation (ANSTO), Australia. KOALA is a vertical-axis Laue diffractometer situated at the end of a thermal-neutron guide. The incoming polychromatic neutron beam, which has a Maxwellian distribution with wavelengths from ~ 0.5 to 4.5 Å, was reduced to 0.8 – 1.7 Å using beam choppers (Piltz 2018a), and diffracted by the sample onto neutron sensitive image plate detectors that surround the sample position in a cylindrical geometry extending ± 144° in the horizontal and ± 52° in the vertical directions. Sample data were collected at 300 and 100 K (using the standard CF-2 cryostat on KOALA), at a total of 33 sample positions. The total collection time for each dataset lasted ~ 3 days. Reflection intensities were corrected for extinction and absorption using the LAUEG program following the methodology of (Piltz 2018b). Subsequent structure refinement was performed using Jana2006.

RESULTS

Spectroscopy and water content

Raman spectra collected from the sample consist of a doublet at ~ 796 and 841 cm^{-1} and broad peak(s) between 192 and 238 cm^{-1} (figure 2a), features which are very similar to previous ringwoodite spectra (Kleppe et al., 2002). The collected spectra were otherwise unremarkable, with no significant water related peaks observed between 3000-4000 cm^{-1} (figure 2b).

As observed for other OH-bearing ringwoodite samples, the FTIR spectra of samples in this study are dominated by an extremely broad absorption band caused by O-H stretching modes extending from ~ 2000 – 4000 cm^{-1}. This O-H band can be de-convolved into five, or more, symmetric peak contributions centred at 2512, 2854, 3124, 3399 and 3653 cm^{-1} (figure 2c). This suggests the presence of multiple defect-related hydrogen positions in the ringwoodite structure, as discussed later. Water concentration in the sample was quantified by integrating the area beneath the background corrected absorption spectrum from 2000 – 4000 cm^{-1} and applying the Beer-Lambert law, $\varepsilon = (A_i \times 1.8)/(d \times \rho \times c_{H_2O})$, where ε is the absorption coefficient (in $L.mol^{-1}cm^{-2}$), A_i = three times the integrated absorption between 2000 and 4000 cm^{-1}, d is sample thickness in cm, ρ is density (in $g.cm^{-3}$) and c_{H_2O} is the concentration of H_2O in the sample (in wt.%). As absorption coefficients vary significantly between, and within, individual literature studies (Libowitzky and Rossman 1997; Thomas et al. 2015) we have assumed that a weighted average using a range of coefficients will provide a more accurate estimate of water concentration in the samples. Assuming uncertainties in sample thickness of ± 2 μm and reported uncertainties in ε (or ± 20% if not explicitly provided in the relevant publication) we calculate the ringwoodite samples studied contain between 0.84(16) and 1.32(25) wt.% H_2O (table 1, figure 3). The weighted average water concentration in the studied samples, including the water content estimated using EPMA (see below), is 1.05 ± 0.08 wt % H_2O.

Mössbauer spectroscopy

The SMS spectra (figure 4, table 2) from the ringwoodite sample is dominated by an asymmetric quadrupole doublet (centre shift [CS] ~ 1.03 $mm.s^{-1}$, quadrupole splitting [QS] ~ 2.75 $mm.s^{-1}$), with a smaller second component (CS ~ 0.09 $mm.s^{-1}$, QS ~ 0.55 $mm.s^{-1}$). As expected for the ringwoodite

structure, and following previous interpretations, the dominant doublet (coloured green in figure 4) is assigned to octahedral ferrous iron, i.e. Fe^{2+} substituting for magnesium in octahedral coordination. The smaller second component (blue in figure 4), which is visually similar to previous observations interpreted as a non-specific "charge-transfer" mechanism, is well resolved and consistent with the presence of tetrahedral ferric iron, i.e. Fe^{3+} substituting for Si^{4+} cations (Burns and Solberg 1990). The relative intensity of the two fitted doublet signals, assuming a constant recoil-free fraction, implies a ferric iron concentration on the tetrahedral site of 17.7 ± 2.6 % of the ringwoodite crystal's total iron content (table 2).

Crystal chemistry

The chemical compositions of eight crystals from the experimental run products are reported in Table 3. This confirms the chemical homogeneity between crystals randomly chosen from the run products, and provides a well-characterised composition for constraining diffraction refinements. The average H_2O concentration calculated by difference of EPMA totals from 100% is 1.06 ± 0.45 wt.%, which is in good agreement with FTIR analyses (figure 2, table 3). Compositions for all analyses were reduced to cation formulae by assuming the presence of four oxygens per formula unit (pfu, table 3). The uncertainty in the mean sample composition is reported (to 1σ), and is less than ± 0.01 pfu for all cations.

Following the results from SMS, initial cation site assignments were made assuming that the entire Fe^{3+} content in the ringwoodite was present on the B site (within the general formula $A_2BO_{4-x}.(H_2O)_x$). This suggests a general mineral formula, based on stoichiometric assignments and the assumption that no tetrahedral vacancies are present, of $(Mg_{1.728}Fe^{2+}_{0.146}Si_{0.041}[V]^{A}_{0.085})(Si_{0.967}Fe^{3+}_{0.033})O_{3.915}.(H_2O)_{0.085}$.

Single-crystal diffraction

X-ray diffraction data from ID15B were refined using Jana2006 software in the $Fd\bar{3}m$ space group, with the octahedrally coordinated cations in the 16d sites at 0.5, 0.5, 0.5, the tetrahedrally coordinated

cations in the 8a sites at 0.125, 0.125, 0.125 and the oxygen anions in the 32e sites at (x, x, x ; x~0.25). The overall sample composition was constrained during refinement, using stoichiometric assignments from EPMA as the starting point for refinements and keeping overall chemistry constrained throughout. From this initial state, complete octahedral/tetrahedral order/disorder of Si, Mg and Fe cations was permitted by refinement of site occupancies. It was observed that no Mg disorder was predicted, so this refinement option was removed after initial investigation. Isotropic thermal parameters were constrained to be equal for all atoms occupying each specific crystallographic site; this appears to be common practice for such refinements (e.g. Smyth et al. 2003). The resulting x-ray refinement has the formula $(Mg_{1.728}Fe^{2+}_{0.133(1)}Si_{0.123(2)}[V]^{A}_{0.016})(Si_{0.885(2)}Fe^{3+}_{0.045(1)}[V]^{B}_{0.07})O_4$ (Supplementary Information), implying an Fe^{3+}/Fe^{tot} of 25% if all tetrahedral iron is assumed to be ferric. It is noted that, if the starting point for refinement is changed such that all Mg/Fe cations are in octahedral and all Si in tetrahedral coordination (i.e. 100% ordered cations), the final refined site occupancies do not change significantly from those reported in the supplementary information, and the same minimum is found. The identification of Si-Fe cation disorder, with ~ 12 % Si in octahedral coordination, appears to be reliably constrained in spite of the similarity in scattering factors for Mg and Si (Smyth et al. 2003).

Refinement of the single-crystal Laue neutron diffraction datasets, collected at 100 and 300 K, were undertaken in a similar manner. This resulted in similar results from both neutron datasets; both robustly identifying 8-12 % Si cation disordering onto the octahedral site prior to inclusion of H atoms in refinements (Supplementary Information). We emphasise that the neutron refinements were conducted completely separately from treatment of X-ray diffraction data, and the consistency of cation disorder provides further support for the robustness of this observation. It is also notable that both datasets refine to have between 13 ± 3.3 and 28 ± 2.8 % tetrahedrally coordinated iron, which is comparable with the measured ferric iron content from SMS (17.7 ± 2.6 %). The ringwoodite formulae from the two neutron diffraction refinements, on an anhydrous basis, are $(Mg_{1.728}Fe^{2+}_{0.156(6)}Si_{0.085(14)}[V]^{A}_{0.031})(Si_{0.923(14)}Fe^{3+}_{0.023(6)}[V]^{B}_{0.054})O_4$ and

224 $(Mg_{1.728}Fe^{2+}_{0.129(5)}Si_{0.085(12)}[V]^{A}_{0.058})(Si_{0.922(12)}Fe^{3+}_{0.050(5)}[V]^{B}_{0.028})O_4$ at 300 K and 100 K respectively.
225 In both cases it is implied that hydrogen is present on both tetrahedrally and octahedrally coordinated
226 sites, to charge balance the cation vacancies.

227 Following anhydrous refinement of the neutron datasets, identification of potential hydrogen positions
228 was attempted using Fourier difference maps. This process was conducted by examining difference
229 maps, looking for regions of negative neutron scattering intensity (red colours in Figure 5) that could
230 be caused by the presence of ^{1}H atoms in the ringwoodite structure. Visual inspection of the data
231 revealed many such negative anomalies (Figure 5), and automated peak finding procedures in
232 Jana2006 were used to identify candidate positions. Subsequently, candidate sites were inspected to
233 ensure only physically reasonable positions were chosen. Since at lower temperatures there is reduced
234 thermal energy in the system, and therefore atoms should produce stronger Fourier anomalies, the 100
235 K dataset was examined first.

236 In this case two potential hydrogen positions were identified, one associated with each of the
237 tetrahedral and octahedral sites. Fourier difference maps demonstrate these red peaks of negative
238 scattering intensity associated with the octahedra near the face of the octahedral site, and, for the
239 tetrahedral sites, as negative intensity halfway along each tetrahedral edge (indicated with black arrows
240 in Figure 5a and b respectively). These observations are reminiscent of those described by Purevjav et
241 al. (2018), collected with ToF single crystal neutron diffraction from an iron-free ringwoodite crystal.
242 We further discuss the reliability of this type of observation in both this study and in Purevjav et al.
243 (2018) in a subsequent section, but if both the anomalies observed here are adopted as hydrogen
244 positions in the structure then a successful refinement of their occupancy and U_{iso} alongside other
245 refinement parameters can be achieved. This refinement implies both sites identified are partially
246 occupied, with approximately twice as many hydrogen atoms associated with tetrahedral vacancies
247 than are associated with vacant octahedral sites. We note that the uncertainties in site occupancies are
248 particularly large for the octahedral site (± 107% of the refined total occupancy), but the hydrogen

content of the tetrahedral site has a relative uncertainty of ± 19%. The two hydrogen sites have thermal parameters approximately 2.5-6 times larger than those for the magnesium, iron, silicon and/or oxygen cations, suggesting the hydrogen positions are a diffuse cloud, even at 100K. The total water content, which was unconstrained in the refinement, is predicted to be 1.16 ± 0.61 wt.% H_2O, which is within 2σ uncertainty of the weighted average water content estimate from FTIR. This water-bearing refinement charge balances the overall ringwoodite structure, but does not completely protonate all individual vacancies (i.e. not every $[V]^A$ or $[V]^B$ can be filled with 2 or 4 protons respectively). At face value this refinement result seems reasonable and will be discussed further below.

In the dataset collected at 300 K it is no longer possible to discern a signal that might be associated with ^1H at the tetrahedral site. However, there continues to be a peak, although weaker than at 100K, in negative scattering density associated with the same locations at the octahedral site which can be assigned as hydrogen for refinement (black arrows in Figure 5c). In this case, free refinement of both occupancy and U_{iso} results in a structure containing 2.19 ± 0.55 wt.% H_2O in the octahedral site, with a U_{iso} that is 75% smaller than for any other atom in the structure. Additionally, this refinement results in the octahedral site being 10% overfilled. Given that the temperature has increased, so thermal parameters should have increased (not decreased) from 100 K, and the broad O-H stretch observed in FTIR this seems highly unlikely and is considered to be an unreliable result. Thus, we believe that the neutron diffraction data collected at 300 K are unable to reliably constrain the hydrogen positions in the structure.

DISCUSSION

In contrast with previous studies of iron-bearing ringwoodite samples, our combined results from SMS and diffraction refinements appear to conclusively demonstrate the presence of tetrahedrally co-ordinated ferric iron in the ringwoodite structure. Whilst previous studies have identified elevated ferric iron concentrations in hydrous Fo_{90} ringwoodite when compared with anhydrous samples, these have not been definitively associated with tetrahedral coordination (e.g. McCammon et al. 2004).

Instead, Mössbauer spectroscopy in these studies had assigned the secondary "ferric iron" component as explained by a rapid Fe^{2+}-Fe^{3+} charge transfer mechanism believed to be possible only if the iron was completely in octahedral coordination (e.g. McCammon et al. 2004). Mössbauer spectra presented by Mrosko et al. (2013) did suggest that, after annealing a sample of Fo_{90} ringwoodite in air and observing a colour change in the sample, there was some evidence for a minor component (< 3%) of tetrahedral ferric iron that was consistent with their FTIR spectroscopy. The presence of tetrahedral ferric iron in samples from this study also necessarily demonstrates the presence of cation disorder in the ringwoodite structure as, given the chemistry of the samples analysed by EPMA, it is an inevitable consequence that the tetrahedral ferric iron must displace an equivalent portion of Si atoms onto the octahedral sites. Disorder of silicon onto the octahedral site has been suggested in previous studies via refinement of X-ray data alone, with studies reporting up to 4% Si-Mg exchange between the tetrahedral and octahedral sites (Kudoh et al. 2000). This type of exchange has also often been cited as a potential hydrogen incorporation mechanism (see below). However, neither the confirmation of cation disorder with multiple techniques analysing the same samples nor the involvement of ferric iron in this exchange reaction have previously been documented. Independent X-ray and 2 separate neutron diffraction refinements, as well as SMS results in this study all independently suggest that 13 – 28 % of the iron in these samples is ferric and in tetrahedral coordination. It is unclear whether or not this is a unique result of the synthesis method, but since the crystals were grown with excess water in a welded platinum capsule, as in previous studies, this seems unlikely. More likely, perhaps, is the superiority of synchrotron Mössbauer spectroscopy over a lab approach when analysing small samples synthesised at high-pressure, and the increased capability of neutron diffraction for discrimination of iron, magnesium and silicon compared to X-ray scattering techniques.

The neutron diffraction refinements, presented above, do not unambiguously identify the hydrogen incorporation mechanism in these samples. Thus, in addition to the presented refinements in $Fd\bar{3}m$ symmetry, neutron data were also refined assuming $F\bar{4}3m$, $F4_132$ or $Fd\bar{3}$ space groups in case the presence of hydrogen atoms in ringwoodite, which are more "visible" to neutrons, alters the crystal

symmetry. Ultimately, however, none of these additional refinements positively identified hydrogen sites.

The difficulty in identifying hydrogen positions using neutron diffraction might be explained by considering whether or not a sufficient concentration of ^{1}H is present that features observable in a Fourier map are to be expected. Assuming that oxygen and hydrogen atoms occupy the same volume, equivalent to equal U_{iso}'s, we use the relative coherent neutron scattering lengths of ^{16}O and ^{1}H and the observed Fourier intensity of ^{16}O atoms to estimate the peak Fourier scattering density expected from ^{1}H atoms. Based on the observed peak scattering density from oxygen (~ 26 fm/Å^3), hydrogen atoms completely filling the oxygen sites would be expected to have peak scattering densities of ~ -16.7 fm/Å^3 (ratio of $^{1}H/^{16}O$ coherent scattering lengths * observed ^{16}O peak; (-3.74/5.80)*26). If we assume only one hydrogen incorporation mechanism is present, e.g. all 0.17 H atoms pfu (as determined by EPMA) occupy a single site, then, depending on whether the occupied site is 48-fold, 96-fold or 192-fold (which are the most likely in this study and Purevjav et al. 2014; 2018), the expected peak scattering density from ^{1}H is then -0.47, -0.23 or -0.12 fm/Å^3. In reality it is likely that hydrogen will be more diffusely distributed than oxygen, having a larger U_{iso}, and will additionally be partitioned between multiple sites in the crystal structure. Thus, it is expected that the peak scattering from ^{1}H atoms in difference Fourier maps will be at least 2-4 (and possibly as much as 10) times smaller than these values. Quick inspection of difference Fourier maps from our samples (fig. 5) reveals that there are many features of much larger positive and negative scattering densities than these predicted theoretical values, and that true signals from hydrogen atoms could easily be hidden within the green colours on figure 5. This makes it virtually impossible to argue that visual identification of all ^{1}H atoms using Fourier maps is robust. Successful hydrogen identification is only convincing if proton positions are assigned and successfully refined for occupancy and thermal parameters with reasonable results. An example of this is seen in the case of the tetrahedrally coordinated hydrogen position in the 100 K neutron dataset in this study. However, even in this case, the observed scattering density in the Fourier map is approximately 10 times larger than the expected anomaly, casting doubt on the fidelity

of the refinement. Looking at the proposed octahedral hydrogen sites in this, and previous, studies (Purevjav et al. 2018), we note observed negative scattering densities in Fourier maps are at least 20 times larger than expected, whilst nearby positive scattering peaks of equal, but opposite, magnitude were unexplained. We conclude that the successful identification of H atoms, especially in general crystallographic sites within the ringwoodite structure, is extremely challenging, and we are cautious to avoid similar interpretations here based on neutron data alone.

FTIR and NMR spectroscopy as well as first-principles calculations have all been used to provide additional constraints on hydrogen locations in the ringwoodite structure. We look to previously published studies to provide a framework in which to interpret our FTIR observations, which have frequently identified that hydrogen is likely incorporated in a mixture of protonated cationic defects associated with tetrahedral and octahedral vacancies, as well as via cation disorder mechanisms. On the basis of calculations Blanchard et al. (2009) concluded that simple vacancy defects $[V_{Mg}(OH)_2]^x$ and $[V_{Si}(OH)_4]^x$ most likely explain the lowest (~ 2500-2600 cm^{-1}) and highest (3500-3750 cm^{-1}) frequency O-H stretches observed by FTIR respectively. However, a plethora of cation-disorder related substitutions were suggested, including $[Mg_{Si}(OH)_2]^x$ and $[V_{Mg}(OH)_2Mg_{Si}Si_{Mg}]^x$, and several mechanisms may contribute to the main broad peak observed in γ-Mg_2SiO_4 centred around ~ 3150 cm^{-1}.

Whilst other studies using calculations (Panero 2010) and FTIR spectroscopy (Bolfan-Casanova et al. 2000) alone have also concluded that a mixture of vacancy associated hydrogen incorporation mechanisms likely occur in ringwoodite, neither of these studies assigned FTIR bands to specific defects. Instead, studies using coupled observations from multiple techniques, e.g. FTIR and XRD, FTIR and calculations, or the pressure/temperature evolution of FTIR spectra, have more frequently attempted to assign specific spectroscopic observations. Smyth et al. (2003) and Chamorro Perez et al. (2006) interpreted the main O-H stretch around 3150 cm^{-1} as the expression of hydrogen along the edge of vacant tetrahedral sites. In contrast, Panero et al. (2013), Kudoh et al. (2000), Ross et al.

(2003) and Mrosko et al. (2013) have all favoured a model where the broad 3150 cm^{-1} stretch is associated with octahedral vacancies $[V_{Mg}(OH)_2]^x$. The weaker FTIR stretches at higher frequencies between 3500-3700 cm^{-1}, where assigned, are most commonly associated with the tetrahedral vacancy substitution (Mrosko et al. 2013). Studies investigating the temperature and/or pressure dependence of FTIR spectra clearly identify that multiple H-incorporation mechanisms are required to explain peaks following different pressure/temperature evolution (Chamorro Pérez et al. 2006; Mrosko et al. 2013; Panero et al. 2013; Yang et al. 2014). Interpretation of NMR spectra collected from a hydrous iron-free ringwoodite sample (Grüninger et al. 2017) also requires multiple H-sites in ringwoodite. Grüninger et al. (2017) concluded that the substitution into octahedral vacancies was the most dominant hydrogen incorporation mechanism, presumably explaining the large 3150 cm^{-1} stretch, but also identified that up to ~ 50% of the hydrogen was incorporated in tetrahedral and cation disorder related defects. With one exception, Mrosko et al. (2013), none of these studies have interpreted the FTIR spectra of iron-bearing ringwoodite samples specifically in terms of iron-bearing defects.

Although FTIR spectra from iron-free and iron-bearing hydrous ringwoodite samples are broadly similar, they possess subtle, yet important, differences (e.g. Smyth et al. 2003). FTIR spectra of iron-free ringwoodite consist of a dominant peak centred around 3100 cm^{-1} with a full-width-at-half-maximum height (fwhm) of ~ 400 cm^{-1}. Additional small peaks occur around ~ 2500-2600 cm^{-1} and 3700 cm^{-1} in samples with high water content. FTIR spectra of Fo_{90} ringwoodite, like that in this study (fig 2b), consist a much broader central peak (~ 3150 cm^{-1}, fwhm > 600 cm^{-1}) with a distinctive high frequency shoulder (~ 3400 cm^{-1}); this can readily be deconvolved into multiple components. Additionally, the contribution at the highest frequencies (~ 3650 cm^{-1}) is much more significant, whilst the peak at ~ 2500-2600 cm^{-1} appears visibly similar to iron-free samples. Thus, it seems logical that the additional FTIR contribution at ~ 3400 cm^{-1} is associated with a new defect mechanism only occurring in iron-bearing samples. The relative increase in intensity and downward frequency shift of the peak at ~ 3650 cm^{-1} presumably also has some contribution from the presence of iron in ringwoodite's structure. Using optical and FTIR spectroscopy Mrosko et al. (2013) identified that

heating of a Fo_{90} ringwoodite crystal above 773 K, at ambient-pressure, caused irreversible water loss and conversion of ferrous to ferric iron. This process caused the area of the broad 3150 cm^{-1} stretch to decrease (in their study), presumably explained by a drop in $[V_{Mg}(OH)_2]^x$ concentration, whilst the area under peaks at higher frequencies (~ 3650 cm^{-1} and 3450 cm^{-1}) increased. These are the two peaks we suggest are likely to be associated with ferric iron. Given that the peak, or shoulder, at 3400-3450 cm^{-1} is only observed in iron-bearing samples and is known to increase with increasing Fe^{3+}, we propose that this component arises directly from hydrogen incorporation associated with tetrahedrally co-ordinated ferric iron. The second peak at 3650 cm^{-1}, as it is present - although at slightly higher frequencies (~ 3700-3750 cm^{-1}) - in Fo_{100} ringwoodite is perhaps related to a change in O-H bond length associated with the presence of iron, and following the interpretation of Mrosko et al. (2013) we suggest this is due to the expanded iron-bearing octahedra shortening O-H bond lengths in adjacent tetrahedra.

Based on the discussion above, we believe that there is evidence for at least four different hydrogen substitution mechanisms in the samples investigated in this study. This interpretation is consistent with the results from ^1H NMR (Grüninger et al. 2017). The four sites, with their assumed associated FTIR shifts, are (i) hydrogen sites associated with octahedral vacancies (3125 cm^{-1}), (ii) hydrogen associated with tetrahedral vacancies (~ 3650 cm^{-1}), (iii) hydrogen associated with ferric iron disorder onto the tetrahedral site (~ 3400 cm^{-1}) and presumably (iv) hydrogen associated with disordered silicon on the octahedral site (2510/2850 cm^{-1}). We assume that mechanisms (i) and/or (iv) and (ii) and/or (iii) are associated with the octahedral and tetrahedral hydrogen sites observed in the 100 K neutron diffraction refinement respectively. We also note that the presence of multiple sites may explain why the identification of hydrogen from refinement of single-crystal neutron diffraction patterns is particularly problematic.

IMPLICATIONS

Assuming the Earth's interior composition is approximately pyrolitic, we expect ringwoodite to be the dominant chemical component throughout the lower portion of the transition zone (e.g. Ringwood 1968). There is direct evidence, in the form of an exhumed diamond-hosted ringwoodite inclusion found in a Brazilian diamond, that at least one natural ringwoodite sample is hydrous. If the samples examined throughout this study are in any way representative of the mantle ringwoodite component then there are a few interesting consequences. In addition to the possibility that the incorporation of water in ringwoodite significantly lowers its seismic velocities (Jacobsen 2006; Schulze et al. 2018), and therefore allowing mantle water contents to potentially be "mapped" using geophysical techniques, the observation in this study that water could promote primary cation disorder in the ringwoodite structure may amplify these effects. Panero et al. (2008), using first principles calculations, demonstrated that the presence of cation disorder in the ringwoodite structure may cause anomalous, and otherwise unpredicted, softening of the elastic moduli. Panero et al.'s (2008) calculations predict that ringwoodite's acoustic velocities (v_p and v_s) will be between 1 and 2% slower at transition zone conditions as a consequence of ~ 4% Si disorder onto the octahedral site when compared with a fully ordered structure. Given we observe ~ 8-12% disorder in ringwoodite, due to a Si-Fe^{3+} substitution that is seemingly promoted in the presence of water, it may be expected that ringwoodite's velocities would be reduced by 2-6% more than currently expected in regions of the mantle that are hydrated. Alternatively, observed reductions in transition zone velocities might be explained by smaller concentrations of H_2O than currently believed to be present, and mantle water content may be overestimated if the contribution of Si disorder is ignored.

The samples analysed in the present study have a deep royal blue colouration, typical of iron-bearing hydrous ringwoodites. The origin of blue colouration in ringwoodite and other high-pressure ferromagnesian silicates is currently uncertain, having been attributed to light scattering (e.g., Lingemann and Stöffler, 1998; Nagy et al. 2011), or intervalence charge transfer (e.g., Taran et al. 2009). Iron-bearing magnesian ringwoodite can vary in colour from colourless through pale green to deep blue/purple. Ringwoodites studied using optical and near-infrared spectroscopy possess

absorption bands in the visible spectrum that have been attributed to electronic transitions in octahedrally-coordinated Fe^{2+} (8000-12000 cm^{-1}) and/or Fe^{2+}-Fe^{3+} intervalence charge transfers that are centred on green wavelengths around 16000-18000 cm^{-1} (Keppler and Smyth, 2005; Taran et al. 2009). It appears that previous samples tend towards a pale green, rather than blue, colour when synthesised under more reducing conditions (Taran et al. 2009). In this study we also observed, at least in one case, that a sample we synthesised under water-free conditions (confirmed by IR spectroscopy) was also pale green. This anhydrous sample, which also contained excess ferropericlase, did not appear to contain tetrahedrally-coordinated ferric iron (Supplementary figure 1). This implies that the blue colouration in ringwoodite and, by extension, other high-pressure hydrous iron-magnesium silicates which sometimes show similar royal blue colouration, including Phase E (Crichton et al. 1999, Crichton and Ross 2000) and Phase A (personal comm. D. Dobson), could be related to the presence of a combined ferric iron-proton defect. As crystal-field electronic transitions are spin-disallowed for Fe^{3+}, the blue colouration could instead be related to intervalence charge transfers, supporting the assignment of absorption bands by Taran et al. (2009). While strong blue colouration is not a common feature of Fe^{2+}-Fe^{3+} charge transfer in low-pressure silicates, it is clearly the cause of blue in vivianite, ($Fe_3(PO_4)_2.8H_2O$), as discussed in Burns (1981). A question remains regarding why the charge transfer absorption band moves to higher frequencies in ringwoodite compared to low-pressure silicates where it typically occurs around 12000-15000 cm^{-1}. The presence of Fe^{3+} in tetrahedral coordination, combined with its absence from octahedral sites in the present study, would make ringwoodite a class I mixed-valence compound where intervalence-charge transfer, between structurally dissimilar Fe^{2+} and Fe^{3+} sites, would ordinarily occur beyond the visible band. It is possible that proton delocalisation enhances additional charge transfer, by providing fluctuations in local charge environments. Whilst we believe the observations in the present study suggest that the presence of a tetrahedrally coordinated Fe^{3+}-H^+ defect in ringwoodite might be related to its blue colouration, further work is required to verify this.

ACKNOWLEDGEMENTS

We acknowledge the support of UKRI grants NE/P017657/1, NE/M00046X/1 and ST/K000934/1 awarded to Thomson, Brodholt and Wood respectively. We thank Dr Benjamin Buse from the University of Bristol for assisting with EPMA analyses and data reduction. The ESRF is thanked for the provision of in-house research time at ID15B and to Dr Michael Hanfland who provided the facility.

REFERENCES

Blanchard, M., Balan, E., and Wright, K. (2009) Incorporation of water in iron-free ringwoodite: A first-principles study. American Mineralogist, 94, 83–89.

Bolfan-Casanova, N., Keppler, H., Science, D.R.E.A.P., 2000 (2000) Water partitioning between nominally anhydrous minerals in the MgO–SiO_2–H2O system up to 24 GPa: implications for the distribution of water in the Earth's mantle. Earth and Planetary Science Letters, 182, 209–221.

Bolfan-Casanova, N., Schiavi, F., Novella, D., Bureau, H., Raepsaet, C., Khodja, H., and Demouchy, S. (2018) Examination of water quantification and incorporation in transition zone minerals: Wadsleyite, ringwoodite and phase D using ERDA (elastic recoil detection analysis). Frontiers in Earth Science, 6, 354.

Burns, R.G., and Solberg, T.C. (1990) ^{57}Fe-Bearing Oxide, Silicate, and Aluminosilicate Minerals: Crystal Structure Trends in Mossbauer Spectra. *In* L.M. Coyne, S. W. S. McKeever and D. F. Blake (eds) Spectroscopic Characterization of Minerals and Their Surfaces. ACS Symposium Series, Vol 415. American Chemical Society.

Burns, R.G. (1981) Intervalence transitions in mixed valence minerals of iron and titanium. Annual Review of Earth and Planetary Sciences, 9, 345–383.

Chamorro Pérez, E.M., Daniel, I., Chervin, J.C., Dumas, P., Bass, J.D., and Inoue, T. (2006) Synchrotron IR study of hydrous ringwoodite (γ-Mg_2SiO_4) up to 30 GPa. Physics and Chemistry of Minerals, 33, 502–510.

Crichton, W.A. and Ross, N.L. (2000) Equation of state of phase E. Mineralogical Magazine, 64, 561-567.

Crichton, W.A., Ross, N.L., and Gasparik, T. (1999) Equations of state of magnesium silicates anhydrous B and superhydrous B. Physics and Chemistry of Minerals, 26, 570–575.

Dziewonski, A.M., and Anderson, D.L. (1981) Preliminary reference Earth model. Physics of the Earth and Planetary Interiors, 25, 297–356.

Fei, H., and Katsura, T. (2020) High water solubility of ringwoodite at mantle transition zone temperature. Earth and Planetary Science Letters, 531, 115987.

Fei, H., Yamazaki, D., Sakurai, M., Miyajima, N., Ohfuji, H., Katsura, T., and Yamamoto, T. (2017) A nearly water-saturated mantle transition zone inferred from mineral viscosity. Science Advances, 3, e1603024.

Grüninger, H., Armstrong, K., Greim, D., Boffa Ballaran, T., Frost, D.J., and Senker, J. (2017) Hidden Oceans? Unraveling the Structure of Hydrous Defects in the Earth's Deep Interior. Journal of the American Chemical Society, 139, 10499–10505.

Houser, C. (2016) Global seismic data reveal little water in the mantle transition zone. Earth and Planetary Science Letters, 448, 94–101.

Huang, X., Xu, Y., and Karato, S.-I. (2005) Water content in the transition zone from electrical conductivity of wadsleyite and ringwoodite. Nature, 434, 746–749.

Hustoft, J., Amulele, G., Ando, J.I., Otsuka, K., Du, Z., Jing, Z., and Karato, S.-I. (2013) Plastic deformation experiments to high strain on mantle transition zone minerals wadsleyite and ringwoodite in the rotational Drickamer apparatus. Earth and Planetary Science Letters, 361, 7–15.

Inoue, T., Yurimoto, H., and Kudoh, Y. (1995) Hydrous modified spinel, $Mg_{1.75}SiH_{0.5}O_4$: a new water reservoir in the mantle transition region. Geophysical Research Letters, 22, 117–120.

Jacobsen, S.D. (2005) A systematic study of OH in hydrous wadsleyite from polarized FTIR spectroscopy and single-crystal X-ray diffraction: Oxygen sites for hydrogen storage in Earth's interior. American Mineralogist, 90, 61–70.

Jacobsen, S.D. (2006) Effect of Water on the Equation of State of Nominally Anhydrous Minerals. Reviews in Mineralogy and Geochemistry, 62, 321–342.

Karato, S.-I., and Wu, P. (1993) Rheology of the upper mantle: A synthesis. Science, 260, 771–778.

Keppler, H., and Smyth, J.R. (2005) Optical and near infrared spectra of ringwoodite to 21.5 GPa: Implications for radiative heat transport in the mantle. American Mineralogist, 90, 1209–1212.

Kleppe, A.K. (2002) On protons, iron and the high-pressure behavior of ringwoodite. Geophysical Research Letters, 29, 2021.

Kudoh, Y. (2001) Structural relation of hydrous ringwoodite to hydrous wadsleyite. Physics and Chemistry of Minerals, 28, 523–530.

Kudoh, Y., Kuribayashi, T., Mizobata, H., and Ohtani, E. (2000) Structure and cation disorder of hydrous ringwoodite, γ-$Mg_{1.89}Si_{0.98}H_{0.30}O_4$. Physics and Chemistry of Minerals, 27, 474–479.

Libowitzky, E., and Rossman, G.R. (1997) An IR absorption calibration for water in minerals. American Mineralogist, 82, 1111–1115.

Lingemann, C.M., and Stöffler, D. (1998) New evidence for the colouration and formation of ringwoodite in severely shocked chondrites. LPI, 1308.

McCammon, C.A., Frost, D.J., Smyth, J.R., Laustsen, H.M.S., Kawamoto, T., Ross, N.L., and van Aken, P.A. (2004) Oxidation state of iron in hydrous mantle phases: Implications for subduction and mantle oxygen fugacity. Physics of the Earth and Planetary Interiors, 143, 157–169.

Meier, U., Trampert, J., and Curtis, A. (2009) Global variations of temperature and water content in the mantle transition zone from higher mode surface waves. Earth and Planetary Science Letters, 282, 91–101.

Mrosko, M., Lenz, S., McCammon, C.A., Taran, M., Wirth, R., and Koch-Müller, M. (2013) Hydrogen incorporation and the oxidation state of iron in ringwoodite: A spectroscopic study. American Mineralogist, 98, 629–636.

Munch, F.D., Grayver, A.V., Guzavina, M., Kuvshinov, A.V., and Khan, A. (2020) Joint Inversion of Daily and Long - Period Geomagnetic Transfer Functions Reveals Lateral Variations in Mantle Water Content. Geophysical Research Letters, 47, 185.

Nagy, S., Józsa, S., Gyollai, I., Bérczi, S., Bendő, Z., and Stehlik, H. (2011) Ringwoodite microstructures in L-chondrite NWA 5011: implications for transformation mechanism and source region in L parent body. Central European Geology, 54, 233–248.

Panero, W.R. (2008) Cation disorder in ringwoodite and its effects on wave speeds in the Earth's transition zone. Journal of Geophysical Research B: Solid Earth, 113, 838.

Panero, W.R. (2010) First principles determination of the structure and elasticity of hydrous ringwoodite. Journal of Geophysical Research, 115, 585.

Panero, W.R., Smyth, J.R., Pigott, J.S., Liu, Z., and Frost, D.J. (2013) Hydrous ringwoodite to 5 K and 35 GPa: Multiple hydrogen bonding sites resolved with FTIR spectroscopy. American Mineralogist, 98, 637–642.

Pearson, D.G., Brenker, F.E., Nestola, F., McNeill, J., Nasdala, L., Hutchison, M.T., Matveev, S., Mather, K., Silversmit, G., Schmitz, S., and others (2014) Hydrous mantle transition zone indicated by ringwoodite included within diamond. Nature, 507, 221–224.

Piltz, R.O. (2018a) Accurate data processing for neutron laue diffractometers. Journal of Applied Crystallography, 51, 635–645.

Piltz, R.O. (2018b) LaueG software for displaying and processing neutron laue images. Journal of Applied Crystallography, 51, 963–965.

Potapkin, V., Chumakov, A.I., Smirnov, G.V., Celse, J.P., Rüffer, R., McCammon, C., and Dubrovinsky, L. (2012) The ^{57}Fe Synchrotron Mössbauer Source at the ESRF. Journal of Synchrotron Radiation, 19, 559–569.

Prescher, C., McCammon, C., and Dubrovinsky, L. (2012) MossA: a program for analyzing energy-domain Mössbauer spectra from conventional and synchrotron sources. Journal of Applied Crystallography, 45, 329–331.

Purevjav, N., Okuchi, T., Tomioka, N., Abe, J., and Harjo, S. (2014) Hydrogen site analysis of hydrous ringwoodite in mantle transition zone by pulsed neutron diffraction. Geophysical Research Letters, 41, 6718–6724.

Purevjav, N., Okuchi, T., Wang, X., Hoffmann, C., and Tomioka, N. (2018) Determination of hydrogen site and occupancy in hydrous Mg_2SiO_4 spinel by single-crystal neutron diffraction. Acta Crystallographica Section B: Structural Science, Crystal Engineering and Materials, 74, 115–120.

Ringwood, A.E. (1968) Phase transformations in the mantle. Earth and Planetary Science Letters, 5, 401–412.

Ross, N.L., Gibbs, G.V., and Rosso, K.M. (2003) Potential docking sites and positions of hydrogen in high-pressure silicates. American Mineralogist, 88, 1452–1459.

Schulze, K., Marquardt, H., Kawazoe, T., Boffa Ballaran, T., McCammon, C., Koch-Müller, M., Kurnosov, A., and Marquardt, K. (2018) Seismically invisible water in Earth's transition zone? Earth and Planetary Science Letters, 498, 9–16.

Smyth, J.R. (1987) The beta -Mg_2SiO_4: a potential host for water in the mantle? American Mineralogist, 72, 1051–1055.

Smyth, J.R. (1994) A crystallographic model for hydrous wadsleyite: An ocean in the Earth's interior? American Mineralogist, 79, 1021–1025.

Smyth, J.R., Holl, C.M., Frost, D.J., Jacobsen, S.D., Langenhorst, F., and McCammon, C.A. (2003) Structural systematics of hydrous ringwoodite and water in Earth's interior. American Mineralogist, 88, 1402–1407.

Suetsugu, D., Inoue, T., Obayashi, M., Yamada, A., Shiobara, H., Sugioka, H., Ito, A., Kanazawa, T., Kawakatsu, H., Shito, A., and others (2010) Depths of the 410-km and 660-km discontinuities in and around the stagnant slab beneath the Philippine Sea: Is water stored in the stagnant slab? Physics of the Earth and Planetary Interiors, 183, 270–279.

Taran, M.N., Koch-Müller, M., Wirth, R., Abs-Wurmbach, I., Rhede, D., and Greshake, A. (2009) Spectroscopic studies of synthetic and natural ringwoodite, γ-$(Mg, Fe)_2SiO_4$. Physics and Chemistry of Minerals, 36, 217–232.

Thomas, S.-M., Bina, C.R., Jacobsen, S.D., and Goncharov, A.F. (2012) Radiative heat transfer in a hydrous mantle transition zone. Earth and Planetary Science Letters, 357-358, 130–136.

583 Thomas, S.-M., Jacobsen, S.D., Bina, C.R., Reichart, P., Moser, M., Hauri, E. H., Koch-Müller, M.,
584 Smyth, J. R., and Döllinger, G. (2015) Quantification of water in hydrous ringwoodite. Frontiers in
585 Earth Science, 2, 720–10.

586 van der Meijde, M., Marone, F., Giardini, D., and van der Lee, S. (2003) Seismic Evidence for Water
587 Deep in Earth's Upper Mantle. Science, 300, 1556–1558.

588 Yang, X., Keppler, H., Dubrovinsky, L., and Kurnosov, A. (2014) In-situ infrared spectra of hydroxyl
589 in wadsleyite and ringwoodite at high pressure and high temperature. American Mineralogist, 99,
590 724–729.

591 Ye, Y., Brown, D.A., Smyth, J.R., Panero, W.R., Jacobsen, S.D., Chang, Y.Y., Townsend, J.P.,
592 Thomas, S.M., Hauri, E.H., Dera, P., and Frost, D.J. (2012) Compressibility and thermal
593 expansion of hydrous ringwoodite with 2.5(3) wt% H_2O. American Mineralogist, 97, 573–582.

594 Yoshino, T., Manthilake, G., Matsuzaki, T., and Katsura, T. (2008) Dry mantle transition zone inferred
595 from the conductivity of wadsleyite and ringwoodite. Nature, 451, 326–329.

596

FIGURE CAPTIONS

Figure 1: Photomicrograph of selected ringwoodite crystals recovered from synthesis.

Figure 2: (a) Raman spectra collected in this study, at 1 cm^{-1} and 4 cm^{-1} resolution, compared with a reference spectrum from Kleppe et al. (2002). (b) Raman spectra extended out to 4500 cm^{-1}, covering the spectral region where stretches associated with O-H might be expected. (c) FTIR absorption spectra collected from a single crystal ringwoodite sample at ambient conditions, normalised to 1 cm thickness. Inset: baseline-corrected absorption from 2000 – 4000 cm^{-1}, for H_2O concentration quantification and deconvolved into contributing peaks after Monique-Thomas et al (2016).

Figure 3: Water content of ringwoodite sample based on individual FTIR calibrations, EPMA by difference and an overall weighted average.

Figure 4: Synchrotron Mössbauer spectra collected at ID18, fitted with two spectral components using MossA. Raw data is shown by the black points and the complete model fit by the red curve. The model fit is composed of two components; the green asymmetric doublet is interpreted as the signal from octahedral ferrous iron whilst that highlighted in blue is assigned as tetrahedral ferric iron.

Figure 5: Fourier difference maps from single-crystal Laue neutron diffraction data (with elements of the crystal structure superimposed) which allow visualisation of possible hydrogen positions (a) 110 plane and (b) 100 through 100 K data collection focussed on the (a) octahedral site of Mg, Fe and Si whose relative proportions are indicated by the orange, brown and blue coloured segments respectively, (b) tetrahedral site contain Si and Fe. (c) 110 plane through 300 K data focussed on the octahedral site in $Fd\bar{3}m$ symmetry.

617 **Table 1:** Results of FTIR analysis to determine sample H_2O concentration using various absorption

618 coefficients

Sample	d (µm)		Ai	cH_2O (MT_a)		cH_2O (MT_b)		cH_2O (LR)		cH_2O (MT_c)		cH_2O (BC)	
a	50	*2*	1055.9	0.94	*0.19*	1.06	*0.22*	0.83	*0.17*	1.27	*0.26*	0.78	*0.06*
b	57	*2*	1505.9	1.17	*0.24*	1.33	*0.27*	1.04	*0.21*	1.59	*0.32*	0.97	*0.07*
c	42	*2*	760.6	0.81	*0.17*	0.91	*0.19*	0.71	*0.15*	1.09	*0.22*	0.67	*0.05*
average				0.97	*0.20*	1.10	*0.22*	0.86	*0.18*	1.32	*0.27*	0.81	*0.06*

619 Numbers in italics are estimated uncertainties in thickness and water content measurements.
620 MT_a (ε = 111,815 $L.mol^{-1}cm^{-2}$) (Thomas et al. 2015)
621 MT_b (ε = 98,830 $L.mol^{-1}cm^{-2}$) (Thomas et al. 2015)
622 LR (ε = 126,393 $L.mol^{-1}cm^{-2}$) (Libowitzky and Rossman 1997)
623 MT_c (ε = 82,640 ± 16,530 $L.mol^{-1}cm^{-2}$) (Thomas et al. 2015)
624 BC (ε = 135,133 ± 8,794 $L.mol^{-1}cm^{-2}$) (Bolfan-Casanova et al. 2018)
625

626

627 **Table 2:** Fitting parameters from SMS spectra of sample crystals.

	Intensity	CS (mm/s)	QS (mm/s)
Fe^{2+}	82.3 ± 2.6	1.030 ± 0.005	2.757 ± 0.009
Fe^{3+}	17.7 ± 2.6	0.091 ± 0.076	0.551 ± 0.086

628

This is the peer-reviewed, final accepted version for American Mineralogist, published by the Mineralogical Society of America.
The published version is subject to change. Cite as Authors (Year) Title. American Mineralogist, in press.
DOI: https://doi.org/10.2138/am-2021-7539. http://www.minsocam.org/

Table 3: EPMA analyses, in wt.%, of synthetic ringwoodite crystals, assuming Fe^{3+}/Fe^{tot} from SMS measurements and H_2O by difference

	Wt.% oxides							Atoms per 4 oxygens (pfu)						
crystal	SiO_2	FeO	Fe_2O_3	MgO	Total	H_2O		Si	Fe^{2+}	Fe^{3+}	Mg	H	O	Mg#
a	41.81	7.51	1.88	47.75	98.95	1.05		1.009	0.152	0.034	1.719	0.171	4	0.90
	41.54	7.43	1.86	47.63	98.46	1.54		1.008	0.151	0.034	1.722	0.172	4	0.90
b	41.99	7.49	1.87	47.76	99.11	0.89		1.012	0.151	0.034	1.715	0.171	4	0.90
	41.63	7.50	1.88	48.05	99.07	0.93		1.005	0.151	0.034	1.728	0.171	4	0.90
	41.65	7.43	1.86	47.63	98.56	1.44		1.009	0.150	0.034	1.720	0.172	4	0.90
	41.98	7.38	1.84	47.84	99.04	0.96		1.011	0.149	0.033	1.718	0.171	4	0.90
c	41.24	6.90	1.72	47.99	97.85	2.15		1.004	0.140	0.032	1.742	0.173	4	0.91
	41.94	6.70	1.67	48.76	99.07	0.93		1.007	0.134	0.030	1.745	0.170	4	0.91
	42.26	6.76	1.69	48.84	99.55	0.45		1.009	0.135	0.030	1.739	0.169	4	0.91
	41.89	6.89	1.72	47.77	98.26	1.74		1.014	0.139	0.031	1.724	0.172	4	0.91
d	41.89	7.13	1.78	48.19	99.00	1.00		1.009	0.144	0.032	1.730	0.171	4	0.91
	41.52	7.16	1.79	48.33	98.79	1.21		1.003	0.145	0.033	1.740	0.171	4	0.91
	41.41	7.02	1.76	47.97	98.16	1.84		1.005	0.143	0.032	1.736	0.172	4	0.91
e	41.70	7.16	1.79	47.86	98.51	1.49		1.009	0.145	0.033	1.727	0.172	4	0.91
f	41.92	6.84	1.71	48.95	99.42	0.58		1.004	0.137	0.031	1.747	0.170	4	0.91
g	42.15	7.03	1.76	48.21	99.14	0.86		1.012	0.141	0.032	1.726	0.170	4	0.91
	41.99	7.17	1.79	48.35	99.31	0.69		1.008	0.144	0.032	1.730	0.170	4	0.91
	42.07	7.12	1.78	48.08	99.06	0.94		1.012	0.143	0.032	1.724	0.171	4	0.91
h	42.01	7.56	1.89	47.96	99.42	0.58		1.010	0.152	0.034	1.718	0.170	4	0.90
	41.74	7.62	1.91	48.13	99.39	0.61		1.004	0.153	0.035	1.726	0.171	4	0.90
	41.61	7.71	1.93	47.74	98.98	1.02		1.006	0.156	0.035	1.721	0.171	4	0.90
	41.57	7.66	1.92	47.81	98.96	1.04		1.005	0.155	0.035	1.723	0.171	4	0.90
	42.02	7.41	1.85	48.20	99.49	0.51		1.008	0.149	0.033	1.724	0.170	4	0.90
Mean	41.80	7.24	1.81	48.08	98.94	1.06		1.008	0.146	0.033	1.728	0.171	4	0.91
± (1σ)	0.25	0.30	0.08	0.37	0.45	0.45		0.003	0.006	0.001	0.009	0.001		0.00

This is the peer-reviewed, final accepted version for American Mineralogist, published by the Mineralogical Society of America.
The published version is subject to change. Cite as Authors (Year) Title. American Mineralogist, in press.
DOI: https://doi.org/10.2138/am-2021-7539. http://www.minsocam.org/

Figure 1

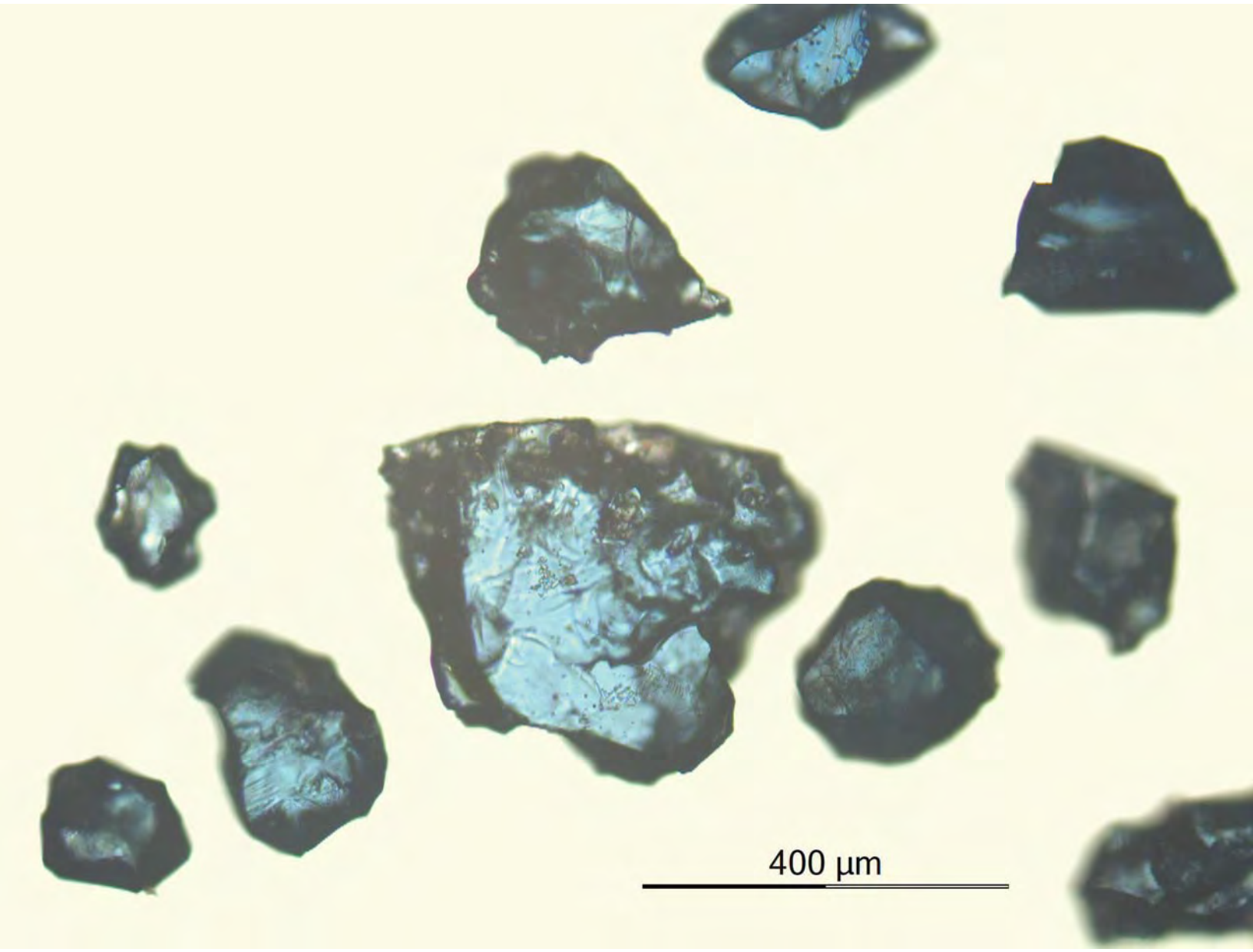

Figure 2

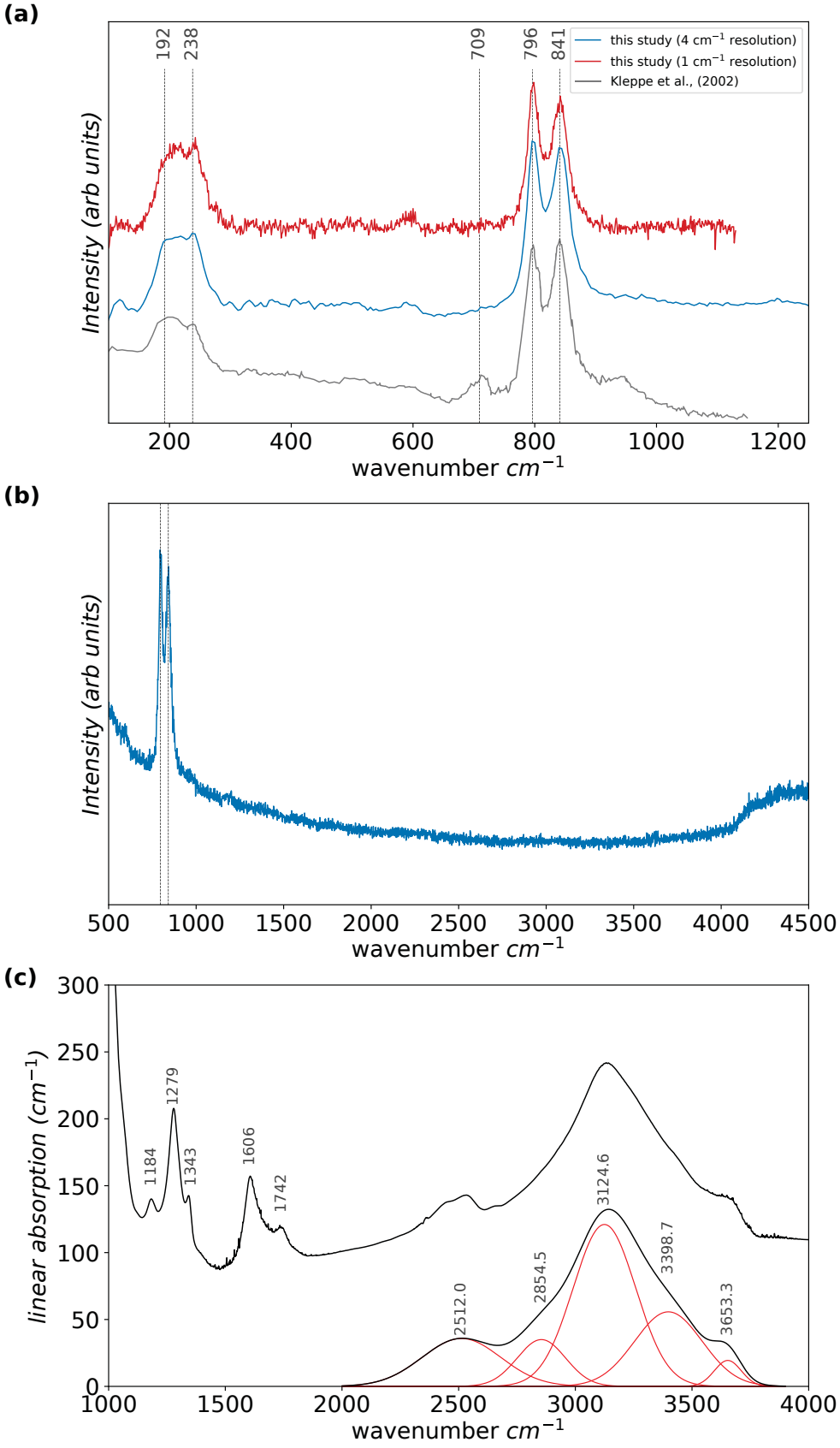

Figure3

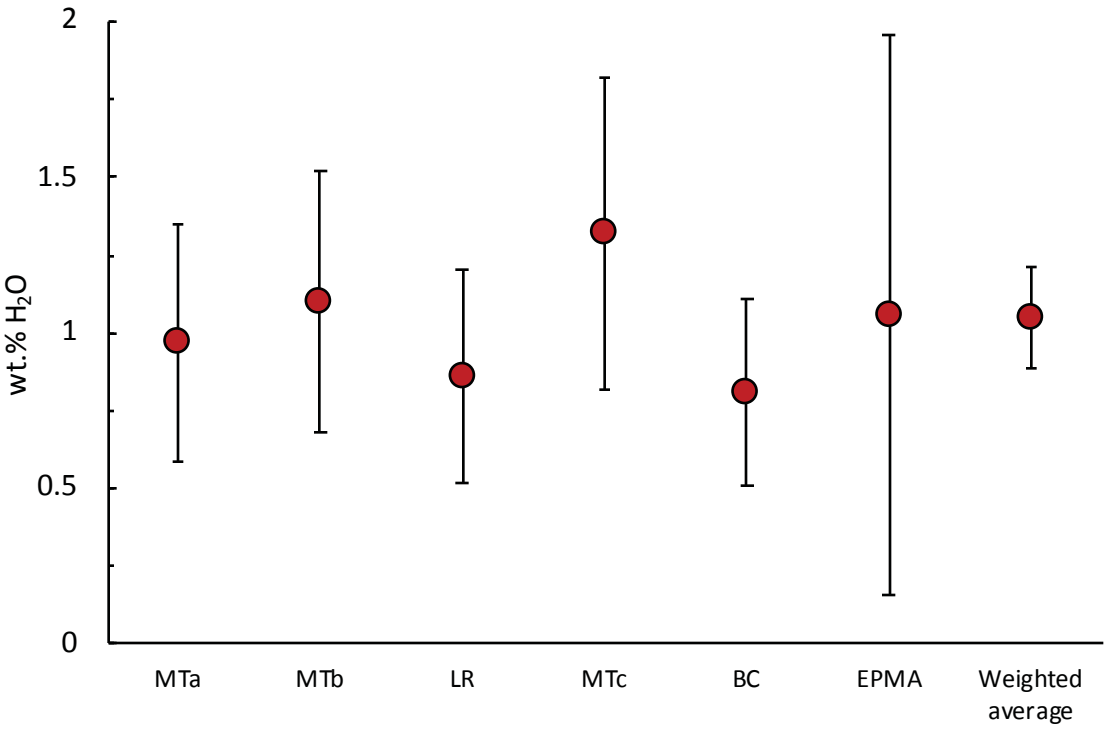

This is the peer-reviewed, final accepted version for American Mineralogist, published by the Mineralogical Society of America.
The published version is subject to change. Cite as Authors (Year) Title. American Mineralogist, in press.
DOI: https://doi.org/10.2138/am-2021-7539. http://www.minsocam.org/

Figure 4

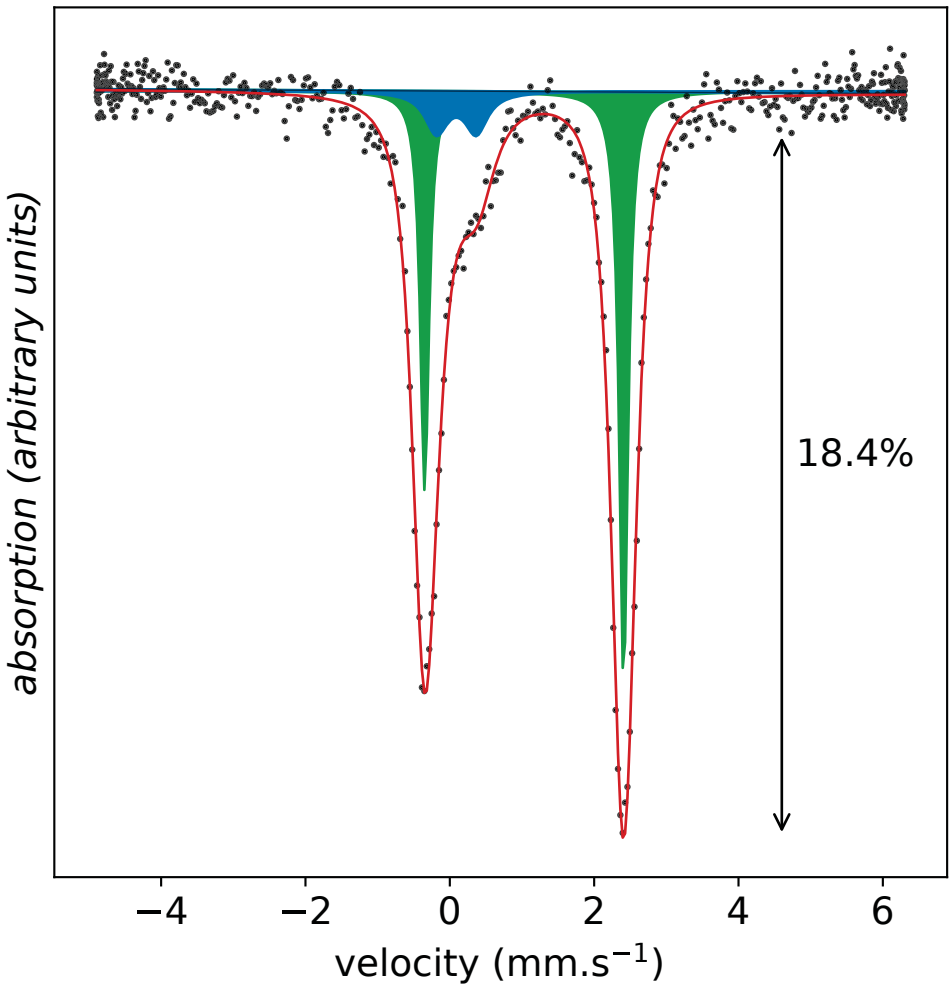

This is the peer-reviewed, final accepted version for American Mineralogist, published by the Mineralogical Society of America.
The published version is subject to change. Cite as Authors (Year) Title. American Mineralogist, in press.
DOI: https://doi.org/10.2138/am-2021-7539. http://www.minsocam.org/

Figure 5